Adv Comput Math (2015) 41:663–689
DOI 10.1007/s10444-014-9382-z

Multilevel approximation of the gradient operator on an adaptive spherical geodesic grid

Ratikanta Behera · Mani Mehra · N. K.-R. Kevlahan

Received: 13 March 2013 / Accepted: 20 October 2014 /
Published online: 12 November 2014

Abstract This work presents a new adaptive multilevel approximation of the gradient operator on a recursively refined spherical geodesic grid. The multilevel structure provides a simple way to adapt the computation to the local structure of the gradient operator so that high resolution computations are performed only in regions where singularities or sharp transitions occur. This multilevel approximation of the gradient operator is used to solve the linear spherical advection equation for both time-independent and time-dependent wind field geophysical test cases. In contrast with other approximation schemes, this approach can be extended easily to other curved manifolds by choosing an appropriate coarse approximation and using recursive surface subdivision. The results indicate that the adaptive gradient calculation and the solution of spherical advection equation accurate, efficient and free of numerical dispersion.

Keywords Second generation wavelet · Gradient operator on the sphere · Spherical geodesic grid · Advection equation · Adaptive wavelet collocation method

Mathematics Subject Classifications (2010) 65T60 · 65DXX

Communicated by: Robert Schaback

R. Behera · M. Mehra (✉)
Department of Mathematics, Indian Institute of Technology Delhi, Delhi, India
e-mail: mmehra@maths.iitd.ac.in

R. Behera
e-mail: ratikanta@maths.iitd.ac.in

N. K.-R. Kevlahan
Department of Mathematics and Statistics, McMaster University, Hamilton, Canada
e-mail: kevlahan@mcmaster.ca

1 Introduction

Many physical systems are characterized by a wide range of active spatial and temporal scales. In addition, applications in geophysics and medicine require tools for analyzing data on a sphere or on other regular closed surfaces [1, 2]. These tools often rely on computing the gradient of a function defined on the curved surface. Numerical approximation of the gradient on the sphere is also necessary to model the tropical atmosphere [3], for transportation problems [4], in image processing [5] and in computer vision [6]. Moreover, in image processing gradient operators are used in the detection of edges and for estimating their local orientation. In medical imaging [7], gradients are used to estimate the direction of surface normals when processing volumetric data. Gradients are also required to evaluate the source term in turbulence models, such as large eddy simulation (LES). In this paper we introduce a new way to approximate the gradient operator on the sphere for functions containing localized small scale structure (i.e. sharp transitions). This approach is adaptive, computationally efficient, and does not suffer from numerical dispersion.

Operational models in atmospheric physics, meteorology and climatology are increasingly based on spherical geodesic grids. The main reason for the choice of this grid is its quasi-uniform convergence on the sphere, which avoids the problems associated with the traditional latitude-longitude grid with the approximation of crucial differential operators[8] (e.g. Laplacian, Jacobian, divergence and gradient). Accurate and stable numerical schemes, together with consistent physical parameterizations, are needed for atmospheric simulations. In addition to these requirements, computational efficiency is necessary for long-term simulations, which means higher resolutions should be used only in regions with fine structure. Furthermore, in many situations the small spatial scales are highly localized, and thus efficient solution of the problem requires a locally adapted grid. Wavelets provide a natural way of dealing with this class of problems. Their power lies in the fact that they only require a small number of coefficients to accurately represent smooth functions and large data sets.

Wavelet analysis and approximation is now used in many areas, including signal processing, data and image compression, solution of partial differential equations (PDEs) and modelling multi-scale phenomena. Well-known orthogonal and continuous wavelets include the Daubechies wavelet [9], Coiflets [9], Meyer wavelet [10] and Morlet wavelet [9]. Wavelet transforms developed in the 1980s (so-called first generation wavelets) were constructed in Fourier space using basis functions that are dilations and translations of a single function (the mother wavelet). These wavelets were therefore limited to flat geometries and simple domains. We use Swelden's [11] *second generation* wavelets to overcome these limitations, which allows wavelets to be defined on general curved surfaces.

A dynamically adaptive multilevel wavelet collocation method for the solution of partial differential equations in flat geometry and finite domains was developed by Vasilyev et al. [12, 13]. Adaptive wavelet methods have been developed for other applications in [14–17]. Recently, this adaptive wavelet collocation methods has been extended from flat geometry to spherical geometry by Mehra and

Kevlahan [18] and subsequently extended by [19, 20]. The new adaptive multiscale gradient operator defined here extends the applicability and power of such wavelet methods.

An important application of this new gradient operator approximation is to advection. Since geophysical fluid motions on all scales are dominated by the advection process, the numerical solution to the advection problem is crucial for the overall accuracy of the flow solver. Furthermore, in physical–chemical problems exact discrete conservation of certain physical quantities, such as mass, is highly desirable. In [18] the advection equation on a curved surface was approximated based on the conservation form,

$$\frac{\partial u}{\partial t} + \nabla \cdot (\vec{V} u) = \frac{\partial u}{\partial t} + \nabla \cdot (u \nabla \chi) - J(u, \psi). \tag{1}$$

This representation uses the Helmholtz–Hodge decomposition of the velocity field $\mathbf{V}$ into two scalar potentials, χ and ψ,

$$\vec{V} = \mathbf{k} \times \nabla \psi + \nabla \chi, \tag{2}$$

where $\mathbf{k}$ is the unit vector normal to the surface, ψ is the stream function representing the divergence-free part, and χ is the velocity potential representing the curl-free part. The Jacobian operator is defined by $J(\alpha, \beta) = \mathbf{k} \cdot (\nabla \alpha \times \nabla \beta)$ for arbitrary scalar functions α and β.

Although the flux–divergence form of the advection Eq. 1 is well suited to collocated numerical approximations of the shallow-water equations on the sphere [21], it is computationally expensive as it requires solving two elliptic equations to find the two scalar potentials χ and ψ from the velocity field $\vec{V}$ at each time step. In addition, in [18] we found that it suffers from numerical dispersion when used in the linear advection equation on the sphere. Numerical dispersion is undesirable for advection problems as it leads to large accumulated errors when the equations are integrated over long times. Thus, it is often preferable to approximate the advection operator directly in non-conservation form using the gradient operator,

$$\nabla \cdot (\vec{V} u) = \vec{V} \cdot \nabla u + u \, \nabla \cdot \vec{V}. \tag{3}$$

The objective of this paper is to derive a computationally efficient non-dispersive multilevel wavelet approximation of the gradient operator on an adaptive spherical geodesic grid contrary to [18] where the discrete adaptive approximations of the differential operators were not optimized for particular applications. Therefore, our aim is to correct these shortcomings (mentioned in previous paragraph) by developing a computationally efficient dispersion-free dynamically adaptive implementation of the advection operator suitable for geophysical flows on the sphere. This required developing a new adaptive multi-level discretization of the gradient operator and testing that it is computationally efficient and dispersion free on the sphere. In addition, the adaptive grid must remain stable for long times (i.e. the adaptive grid should be simply translated and not spread or deform when considering the linear advection problem).

In the current paper, wavelets are used to adapt the computational grid (and hence compress the gradient operator), while finite differences are used to approximate gradient operator. The accuracy of both the gradient operator (first and second component) is controlled by a tolerance parameter ϵ. Using standard test cases from [22] we verify that the method indeed eliminates numerical dispersion and, because it is no longer necessary to solve two Poisson problems at each time step, it is far more computationally efficient. An important goal was to ensure that the dynamically adaptive grid properly tracks advected structures, without grid noise or spreading. To address the performance our method furthermore, we consider highly deformed linear advection problems on the sphere [4]. Grid stability and minimization of dispersive errors for advection problems is vital for efficient dynamically adaptive methods over long times and is one of the major contributions of this paper. Further, the strength of this new approximation method is that it can be extended easily to any smooth curved surface (or other complex domains), while retaining the freedom to choose the wavelet basis depending on the application.

This paper is organized as follows. In Section 2 we introduce the construction of the wavelet transform on the multiscale spherical geodesic grid system. The approximation of gradient operator on an adaptive spherical geodesic grid is presented in Section 3. In Section 4 we apply the method to four stationary test cases for gradient operators: (1) an initial condition introduced by Heikes and Randall [21], (2) a Gaussian function as initial condition, and (3) turbulence data. Finally, (4) the multilevel approximation of gradient operator is applied to the solution of the spherical advection equation for both time-independent and time-dependent wind field geophysical test cases.

2 Wavelet transform on the spherical geodesic grid system

Various grid construction methods based on recursive subdivision of the icosahedron have been proposed, for example by Sadourny et al. [23], Williamson [22] and Masuda and Ohnishi [24]. Such geodesic grids have already been used as the basis for simulations of the shallow water equations [21] and reaction–diffusion equations on the sphere [25]. In general, the icosahedron is recursively refined by bisecting edges of the existing grid (i.e. dyadic refinement). However, for large numbers of subdivisions (e.g. greater than eight or nine) the grid becomes increasingly non-uniform, which can lower the convergence rate of interpolation on the grid. To correct this non-uniformity the grid points can be redistributed, or the interpolation and differential operators on the grid can be modified [21].

To construct a spherical geodesic grid (also called icosahedral–hexagonal grid), we begin with a platonic solid (see Fig. 1) with spherical triangular faces. Each triangular face is then subdivided into four smaller spherical triangles. A variety of construction methods have been proposed for spherical geodesic grids [21, 23]. Here we consider only the simplest edge bisection method for which the number of grid points at subdivision level j is $\mathcal{K}^j = 10 \times 4^j + 2$. Each of the

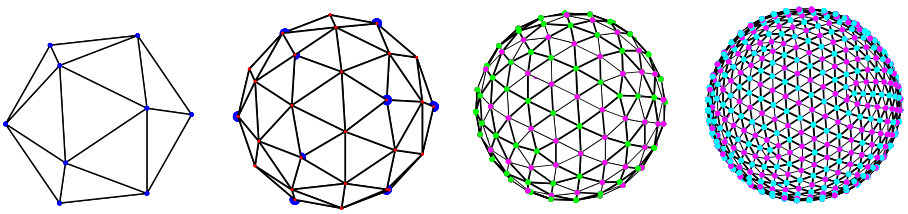

Fig. 1 Geodesic grid generation based on an icosahedron embedded in the sphere

$\mathcal{K}^j$ grid points is surrounded by 6 nearest neighbours except for the original 12 icosahedral vertices which have 5 nearest neighbours (see Fig. 1). The method can be easily modified for the case when the geometry coarse grid has been optimized.

Let $\mathcal{S}$ be a triangulation of the sphere S and denote the set of all vertices obtained after j subdivisions by $\mathcal{S}^j = \{p_k^j \in S | k \in \mathcal{K}^j\}$, where $\mathcal{K}^j$ is an index set, and let q_k^j be the centre of the triangle with vertices $(p_i^j, p_k^j, p_{k+1}^j)$ (see Fig. 2). The original icosahedron $\mathcal{S}^0$ contains only 12 vertices (see Fig. 1 (a)) and $\mathcal{S}^1$ contains those vertices plus all new vertices on the edge midpoints (see Fig. 1 (b)). Since $\mathcal{S}^j \subset \mathcal{S}^{j+1}$ we also let $\mathcal{K}^j \subset \mathcal{K}^{j+1}$. Let $\mathcal{M}^j = \mathcal{K}^{j+1} \setminus \mathcal{K}^j$ be the indices of the vertices added when prolonging the grid from level j to $j+1$ (see Fig. 1).

A second generation multi-resolution analysis (MRA) [11] of the sphere provides a sequence of approximation subspaces $\mathcal{V}^j \subset L_2(S)$ with $j \geqslant 0$ on the sphere $S = \{p = (p_x, p_y, p_z) \in \mathbb{R}^3 : ||p|| = a\}$, where a is the radius of the sphere.

- $\mathcal{V}^j \subset \mathcal{V}^{j+1}$,
- $\bigcup_{j \geq 0} \mathcal{V}^j$ is dense in $L_2(S)$,
- Each $\mathcal{V}^j$ has a Riesz basis of scaling functions $\{\phi_k^j | k \in \mathcal{K}^j\}$.

Since $\phi_k^j \in \mathcal{V}^j \subset \mathcal{V}^{j+1}$, for every scaling function ϕ_k^j filter coefficients $\{h_{k,l}^j\}$ exist such that

$$\phi_k^j = \sum_{l \in \mathcal{K}^{j+1}} h_{k,l}^j \phi_l^{j+1}. \tag{4}$$

Thus, instead of basing the multiresolution analysis on the scaling functions ϕ_k^j it could also be based on the filter coefficients $\{h_{k,l}^j\}$, as long as the set of coefficients admits a solution to Eq. 4 (for details see [12, 26]). Note that the filter coefficients $\{h_{k,l}^j\}$ will in general be different for every $k \in \mathcal{K}^j$ at a given level $j \geqslant 0$ due to the non-uniform geometry of the grid generated by subdivision of the icosahedron. Therefore, each scaling function satisfies a different refinement relation (unlike first generation wavelets, there is no unique mother wavelet). Each MRA is accompanied

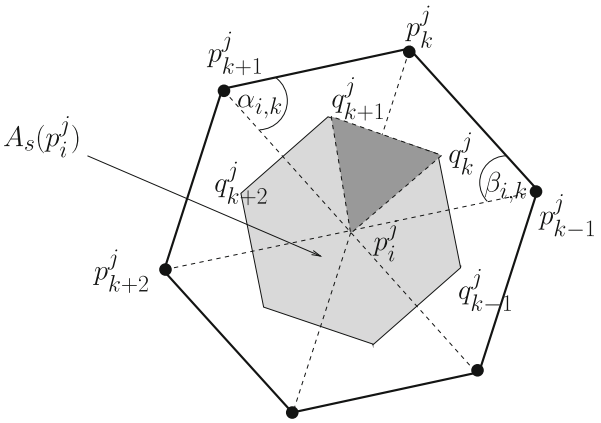

Fig. 2 Schematic figure of angles $\alpha_{i,k}$, $\beta_{i,k}$, neighboring vertices and area A_S

by a dual MRA consisting of nested spaces $\tilde{\mathcal{V}}^j$ spanned by the dual scaling functions $\tilde{\phi}^j_k$, which are biorthogonal to the (primal) scaling functions ϕ^j_k,

$$\langle \phi^j_k, \tilde{\phi}^j_{\acute{k}} \rangle = \delta_{k,\acute{k}}, \text{ for } k, \acute{k} \in \mathcal{K}^j,$$

where $\langle f, g \rangle = \int \int_s fg \, \mathrm{d}w$ is the inner product on the sphere. The dual scaling functions satisfy refinement relations with coefficients $\{\tilde{h}^j_{k,l}\}$.

Wavelet coefficients encode the difference between two successive levels of representation. More precisely, the wavelets form a Riesz basis for the space $\mathcal{W}^j$, which is the complement of $\mathcal{V}^j$ in $\mathcal{V}^{j+1}$ (i.e. $\mathcal{V}^{j+1} = \mathcal{V}^j \bigoplus \mathcal{W}^j$). In our case, the wavelets form a Riesz basis for $L_2(S)$ and allow a function to be represented by its wavelet coefficients. Since $\mathcal{W}^j \subset \mathcal{V}^{j+1}$, we can write

$$\psi^j_k = \sum_{l \in \mathcal{K}^{j+1}} g^j_{k,l} \phi^{j+1}_l,$$

and the spherical wavelets ψ^j_m have $\tilde{d}$ vanishing moments if there exists $\tilde{d}$ linearly independent polynomials $P_i, 0 \leqslant i < \tilde{d}$, such that

$$\langle \psi^j_m, P_i \rangle = 0 \; \forall j \geqslant 0, m \in \mathcal{M}^j,$$

where $\mathcal{M}^j$ is the index set and the polynomials P_i are defined as the restriction to the sphere of polynomials on $\mathbb{R}^3$. The main advantage of the wavelet decomposition is its ability to provide a compressed representation of a large class of functions. For functions which contain isolated small scales on a large scale background, most wavelet coefficients are small. Discarding the small coefficients and reconstructing with the remainder (i.e. nonlinear filtering) provides an efficient multiscale approximation of the original function. In the following Section we derive a new multiscale wavelet method for approximating one of the most important such operators, the gradient operator on the sphere.

3 Adaptive approximation of the gradient operator on a spherical geodesic grid system

Consider a sphere of radius a whose surface is defined by the spherical coordinates (θ, ϕ), where θ $(-\pi \leqslant \theta \leqslant \pi)$ and ϕ $(-\pi/2 \leqslant \phi \leqslant \pi/2)$ are the longitude and latitude respectively. The gradient on the surface of the sphere is given by

$$\nabla_s u = \mathbf{i}\frac{1}{a\cos\phi}\frac{\partial u}{\partial \theta} + \mathbf{j}\frac{1}{a}\frac{\partial u}{\partial \phi},$$

where $\mathbf{i}$ and $\mathbf{j}$ are longitudinal and latitudinal unit vectors respectively.

As mentioned in the introduction, previously, Mehra and Kevlahan [18] approximated the advection operator using the flux–divergence form, where the flux term is calculated in the form of the flux–divergence and Jacobian operators. That form was computationally expensive as it requires solving two elliptic equations to find the χ and ψ from the velocity field $\vec{V}$ see (1). Mehra and Kevlahan also found that this flux–divergence form suffers from some numerical dispersion when used in the linear advection equation on the sphere. Here we approximate the gradient operator directly on an adaptive spherical geodesic grid. This technique is not based on the flux–divergence form, and hence avoids the computationally expensive Helmholtz decomposition into curl-free and divergence-free parts as well as the solution of elliptic equations at each time step.

Let $\mathcal{S}^j$ be the region on the sphere bounded by ∂s. Now, applying the divergence theorem

$$\int_{\mathcal{S}^j} \nabla \cdot \vec{F}\, \mathrm{d}A = \int_{\partial s} \vec{F} \cdot \mathbf{n}\, \mathrm{d}s, \tag{5}$$

where $\vec{F}$ is any vector field on the sphere and $\mathbf{n}$ is the unit outer normal vector to ∂s. Now consider the special case where $\vec{F}$ is the flux of the scalar field u, $\vec{F} = u\vec{C}$, where $\vec{C}$ is a non-zero constant vector field. Then the divergence theorem in Eq. 5 becomes

$$\begin{aligned}\int_{\mathcal{S}^j} \nabla \cdot (u\vec{C})\, \mathrm{d}A &= \int_{\partial s} u\vec{C} \cdot \mathbf{n}\, \mathrm{d}s,\\ &= \vec{C} \cdot \int_{\partial s} u\mathbf{n}\, \mathrm{d}s.\end{aligned} \tag{6}$$

Using the vector identity $\nabla \cdot (u\vec{C}) = (\nabla u) \cdot \vec{C} + u(\nabla \cdot \vec{C})$ in the left hand side of Eq. 6, we can write

$$\begin{aligned}\int_{\mathcal{S}^j} \nabla \cdot (u\vec{C})\, \mathrm{d}A &= \int_{\mathcal{S}^j} [(\nabla u) \cdot \vec{C} + u(\nabla \cdot \vec{C})]\, \mathrm{d}A,\\ &= \vec{C} \cdot \int_{\mathcal{S}^j} \nabla u\, \mathrm{d}A.\end{aligned} \tag{7}$$

Comparing Eq. 6 and Eq. 7 shows that

$$\vec{C} \cdot \int_{\mathcal{S}^j} \nabla u\, \mathrm{d}A = \vec{C} \cdot \int_{\partial s} u\, \mathbf{n}\, \mathrm{d}s,$$

Since $\vec{C}$ is a non-zero constant vector we have

$$\int_{\mathcal{S}^j} \nabla u \, \mathrm{d}A = \int_{\partial s} u\mathbf{n} \, \mathrm{d}s. \tag{8}$$

Let p_i^j be a vertex of the triangulation at level j and let p_k^j, $k \in N(i)$, be the set of nearest neighbour vertices of p_i^j (see Fig. 2).

We now use the finite volume approximation of the gradient operator on the sphere defined in [27]. This method is based on the linear approximation of u at the triangle centroids q_k^j using the values of u at the triangle vertices p_i^j p_k^j p_{k-1}^j and area coordinates,

$$u(q_k^j) = \frac{\alpha\, u(p_i^j) + \beta\, u(p_{k-1}^j) + \gamma\, u(p_k^j)}{\alpha + \beta + \gamma}$$

where α is the area of the triangle q_k^j p_k^j p_{k-1}^j, β is the area of the triangle p_i^j p_k^j q_k^j and γ is the area of the triangle p_i^j q_k^j p_{k-1}^j. u is then approximated at the mid-point of the arc joining triangle centroids q_k and q_{k+1} by linear interpolation as $(u(q_k^j) + u(q_{k+1}))/2$ to give a second-order approximation to the line integrals along the edges of the central hexagon in Fig. 2. The discrete approximation to the gradient operator is then found from Eq. 8 as

$$\nabla u(p_i^j) = \frac{1}{A_s(p_i^j)} \sum_{k \in N(i)} l_k \left[\frac{u(q_k^j) + u(q_{k+1}^j)}{2} \right] \mathbf{n}_k - \frac{u(p_i^j)}{A_s(p_i^j)} \sum_{k \in N(i)} l_k \mathbf{n}_k, \tag{9}$$

where l_k is the length of the arc joining the triangle centroids q_k and q_{k+1}, $\mathbf{n}_k$ is the outward unit normal vector to this arc at its midpoint, and $A_s(p_i^j)$ is the area of the one ring neighbourhood of p_i^j. The control area $A_s(p_i^j)$ can be calculated by the formula given in [28],

$$A_s(p_i^j) = \frac{1}{8} \sum_{k \in N(i)} (\cot \alpha_{i,k} + \cot \beta_{i,k}) \, ||p_k^j - p_i^j||^2,$$

where $\alpha_{i,k}$ and $\beta_{i,k}$ are the angles shown in Fig. 2 and $N(i)$ is the set of nearest neighbour vertices of vertex p_i^j.

The second term on the right hand side of Eq. 9 is a local curvature correction that ensures the gradient of a constant function on the sphere is exactly zero. As noted in [25], however, this correction term is negligible in practice, especially for grids with six or more levels of dyadic refinement. Thus, we will neglect the correction term in the our approximation.

The expression for gradient Eq. 9 can be written compactly in a vector form as

$$\nabla_s u = (G^{1u}, G^{2u}),$$

where G^{1u} and G^{2u} are respectively the longitudinal (first component) and latitudinal components (second component) of the gradient operator.

A function $u(p) \in L_2(S)$ can therefore be represented in terms of its wavelet coefficients as

$$u(p) = \sum_{k \in \mathcal{K}^0} c_k^0 \phi_k^0(p) + \sum_{j=0}^{\infty} \sum_{m \in \mathcal{M}^j} d_m^j \psi_m^j(p). \tag{10}$$

This equation can be written as the sum of two terms composed of wavelets whose amplitudes are respectively above and below some prescribed threshold ϵ, i.e.,

$$u(p) = u_{\geq}(p) + u_{<}(p), \tag{11}$$

$$\text{where } u_{\geq}(p) = \sum_{k \in \mathcal{K}^0} c_k^{J_0} \phi_k^{J_0}(p) + \sum_{j=J_0}^{\infty} \sum_{\substack{m \in \mathcal{M}^j \\ |d_m^j| \geq \epsilon}} d_m^j \psi_m^j(p), \tag{12}$$

$$u_{<}(p) = \sum_{j=J_0}^{\infty} \sum_{\substack{m \in \mathcal{M}^j \\ |d_m^j| < \epsilon}} d_m^j \psi_m^j(p), \tag{13}$$

where J_0 is the coarse level of approximation. Donoho [29] has shown that for smooth enough u,

$$\|u - u_{\geq}\|_{\infty} \leq c_1 \epsilon. \tag{14}$$

The number of significant coefficients $N(\epsilon) = \mathcal{N}$ depends on ϵ,

$$N(\epsilon) \leq c_2 \epsilon^{-n/d}, \tag{15}$$

where d is the order of interpolation, n is the dimension of the problem and the coefficients c_1 and c_2 depend on $u(p)$. Combining relations (14) and (15) gives the following error bound in terms of $N(\epsilon)$

$$\|u - u_{\geq}\|_{\infty} \leq c_3 N(\epsilon)^{-d/n}. \tag{16}$$

Note that d controls the number of zero moments of the interpolating scaling function. This error estimate has been verified numerically for flat geometry [12, 30] and on the sphere [18] .

The estimates Eqs. 14–16 allow us to control both the error of the approximation and the number of wavelet coefficients (i.e. grid points) using only the threshold parameter ϵ. In the present case we use butterfly interpolation [26, 31], which should give fourth-order convergence $d = 4$ provided the grid is sufficiently uniform (i.e. for a moderate number of refinement levels). For very large numbers of the levels the convergence rate of the butterfly interpolation drops to second-order accuracy, $d = 2$, as the bisection refinement leads to a distorted grid near the edges and vertices of the original icosahedron.

Assume that we differentiate locally at a point $p_k^j \in \mathcal{S}^j$ and that h^j characterizes the local grid spacing in all directions at that point. Then, by construction, the local truncation error of the interpolation scheme is $(h^j)^d = O(\epsilon)$. Then approximation of gradient operator will reduce the order of the scheme by one to $(h^j)^{d-1} =$

$O(\epsilon^{d-1/d})$. The convergence rate of the discrete approximation to the gradient operator $G^u_{\geq}$ on the adapted spherical grid to the discrete approximation of the gradient operator on the full spherical grid G^u is therefore

$$||G^u - G^u_{\geq}||_\infty \leq c_5\epsilon^{1-1/d} \leq c_6 N(\epsilon)^{-(d-1)/2}. \tag{17}$$

Note that this convergence rate measures the error due to the wavelet filtering on the adaptive grid when the grid is adapted by filtering the function u rather than ∇u (hence the fact that the error is no longer proportional to ϵ). As mentioned above, we use butterfly interpolation and so we expect that $||G^u - G^u_{\geq}||_\infty \sim \epsilon^{3/4} \sim N(\epsilon)^{3/2}$ for sufficiently uniform grids, and $||G^u - G^u_{\geq}||_\infty \sim \epsilon^{1/2} \sim N(\epsilon)^{1/2}$ for non-uniform grids (i.e. when using a very large number of refinement levels). Recall that the discrete approximation of the continuous gradient operator on the sphere is itself only first-order accurate (i.e. exact for constant functions).

In order to realize the benefits of the wavelet compression, we need to be able to reconstruct ${G^1u}_{\geq}(p)$ from the subset of N grid points (recall Eq. 10 and Eq. 11). Again, we recall that the wavelet coefficients measure the local differences between approximations of a function at two successive levels of resolution j and $j+1$. Thus, if there are no points in the immediate vicinity of a grid point p_i^j (i.e. $d_k^j \leq \epsilon$ for all $k \in N(i)$, and the points $p_i^j, k \in N(i)$, are not present in $\mathcal{S}^{j+1}$) then there exists some neighbourhood Ω_i^j of p_i^j, where the function can be interpolated by a wavelet interpolant based on coefficients $s^j_{k,m}(k \in \mathcal{K}_m)$ to accuracy $O(\epsilon)$,

$$\left| u(p) - \sum_{k\in\mathcal{K}(i)} s^j_{k,m}\phi^j_k(p) \right| \leq c_3\epsilon,$$

where the coefficients $s^j_{k,m}$ can be chosen according as in [18]. After the wavelet decomposition each grid point on the finest level of resolution J is uniquely associated either with a wavelet or with a scaling function at the coarsest level of resolution. Consequently, the collocation point should be omitted from the computational grid if the associated wavelet is omitted from the approximation. For the stability of the reconstruction we must retain all grid points associated with the scaling function at the coarsest level of resolution. This procedure results in a set of nested adaptive computational grids $\mathcal{S}^j_{\geq} \subset \mathcal{S}^j$, such that $\mathcal{S}^j_{\geq} \subset \mathcal{S}^{j+1}_{\geq}$, for any $j < J-1$. Performing the wavelet transform on that adaptive grid guarantees that all wavelet coefficients are exactly the same as those obtained from the wavelet transform of ${G^1u}_{\geq}(p)$ on the complete grid and then setting to zero those wavelet coefficients that do not belong to the adaptive grid. This is the perfect reconstruction criterion. The procedure for adding additional grid points to an adaptive grid, so that the resulting grid satisfies the perfect reconstruction criterion, is called the perfect reconstruction check (for details reconstruction one can see for one and two-dimension in [12, 30] and for sphere in [18]). The grid adaptation algorithm for the first component of gradient operator is described in Algorithm 1. The application of this algorithm is illustrated in the following test cases.

Algorithm 1: GRID ADAPTATION OF THE FIRST COMPONENT OF GRADIENT OPERATOR

- A coarsest level J_0
- A threshold parameter $\epsilon > 0$
- Positive adjacent zone constants M and L

Iterative grid adaptation:
m = 0
$\mathcal{S}_{\geq,m} = \mathcal{S}^{J_0}$
while $m = 0$ or $\mathcal{S}_{\geq,m} \neq \mathcal{S}_{\geq,m-1}$ *or* $||(G^{1u}) - (G^{1u})_{\geq,m}||_\infty > \epsilon$ **do**
  Sample first component of the gradient operator (G^{1u}) on $\mathcal{S}_{\geq,m}$ to give $(G^{1u})_{\geq,m}$.
  m = m+1
  Forward wavelet transform
  Compression: retain only signification coefficients $|d_k^j| \geq \epsilon$ to initialize $\mathcal{S}_{\geq,m}$.
  Reconstruction check:
    add grid points needed to calculate significant coefficients.
    add all points at coarsest level: $\mathcal{S}^{J_0} \subset \mathcal{S}_{\geq,m}$.
  Adaptation: add grid points associated with adjacent zone.
  Inverse wavelet transform: interpolates $(G^{1u})_{\geq,m}$ onto new grid $\mathcal{S}_{\geq,m}$.
Converged result: $\mathcal{S}_{\geq} = \mathcal{S}_{\geq,m}$, $(G^{1u})_{\geq} = (G^{1u})_{\geq,m}$.

4 Results

We verify the multilevel adaptive wavelet approximation of the gradient operator on a spherical geodesic grid by applying it to four complementary test cases. The first test case uses the test function introduced in [21] to verify the error estimate (17) for the second component of the gradient operator. The second test case we uses a Gaussian function on the sphere, and in third test case we apply our method to calculate the gradient of real turbulence data on the sphere. In these two test cases we compute both components of the gradient operator. Finally, the multilevel approximation of gradient operator is applied to the solution of the spherical advection equations in test case 4. Numerical errors are estimated by using L_∞ and L_2 norms computed using the following formulas,

$$||u||_\infty = \max_{k \in \mathcal{K}^j} (|u(p_k^j)|),$$

$$||u||_2 = \left[\frac{1}{\sum_{k \in \mathcal{K}^j} A_s(p_k^j)} \sum_{k \in \mathcal{K}^j} A_s (u(p_k^j))^2 \right]^{1/2}.$$

4.1 Test case 1

Consider the function introduced by Heikes and Randall [21],

$$u(\theta, \phi) = \cos(\theta) \cos^4(\phi). \tag{18}$$

We compute the second component of the gradient operator for the test function (18) and plot ϵ and $N(\epsilon)$ compared to the theoretical prediction $N(\epsilon) \sim \epsilon^{1/2}$ for fourth-order butterfly interpolation derived in Section 3 in Fig. 3. The relation

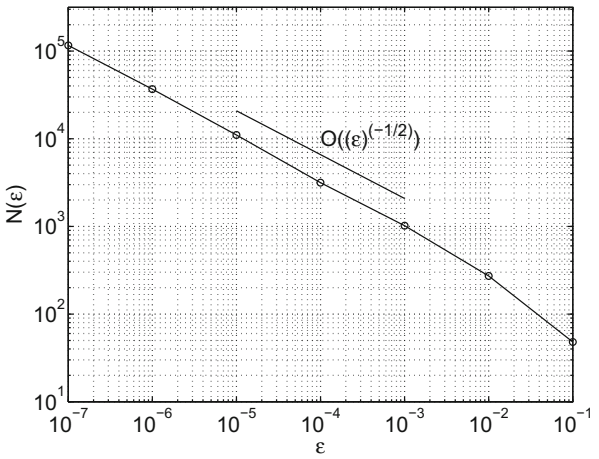

Fig. 3 Scaling of number of active grid points $N(\epsilon)$ with tolerance ϵ for the second component of the gradient operator for test case 1. The results are compared with the theoretical scaling $\epsilon^{-1/2}$

between $||G^{2u} - G^{2u}_{\geq}||_\infty$ and $N(\epsilon)$ is plotted in Fig. 4 (left), and the relation between $||G^{2u} - G^{2u}_{\geq}||_2$ and $N(\epsilon)$ is plotted in Fig. 4 (right). One observes that l_∞ error is of order $O(N(\epsilon)^{-3/2})$ (consistent with fourth-order accurate wavelet interpolation). Again, the relation of $||G^{2u} - G^{2u}_{\geq}||_\infty$ and $||G^{2u} - G^{2u}_{\geq}||_2$ are plotted as a function of ϵ in Fig. 5.

Hence, the approximation of the second component of the gradient operator is indeed controlled by the tolerance ϵ. The second component of the gradient operator is shown in Fig. 6 (left) and the associated adaptive computational grid $G^{2u}{}_{\geq}$ is shown in Fig. 6 (right). The adapted grid is fine only in regions where the function has a strong gradient. Therefore, the adaptive grid clearly reflects the structure of the function. The first component gives similar results.

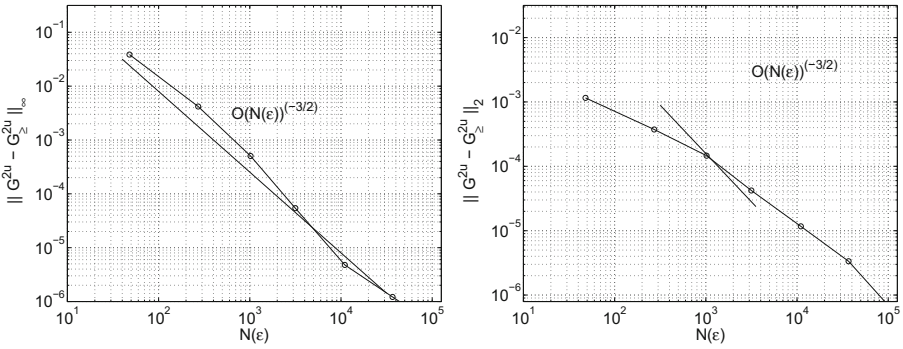

Fig. 4 Scaling of the error in the second component of the gradient operator with number of active grid points $N(\epsilon)$ in the L_∞ (*left*) and L_2 (*right*) norms for test case 1 compared with the theoretical scaling $\epsilon^{-3/2}$

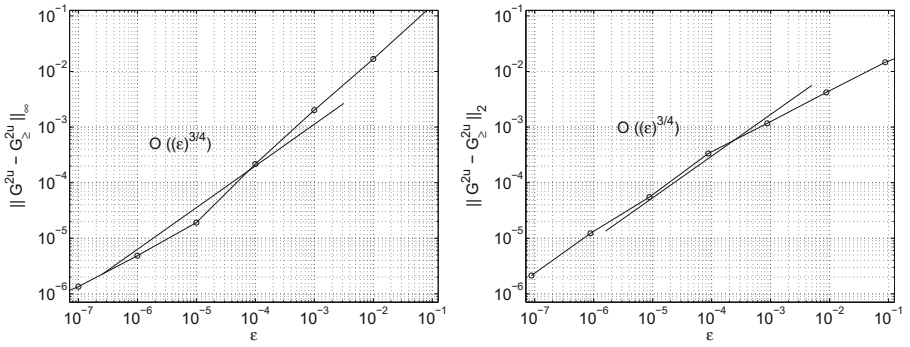

Fig. 5 Control of error for the second component of the gradient operator in the L_∞ (*left*) and L_2 (*right*) norms for test case 1 compared with the theoretical scaling $\epsilon^{3/4}$

In order to demonstrate the efficiency of the multilevel approximation of gradient operator on an adaptive spherical geodesic grid we need to compare the number of grid points used in the adaptive case and the nonadaptive case. This can be measured by the compression coefficient $\mathcal{C} = \frac{\mathcal{N}(\epsilon=0)}{\mathcal{N}(\epsilon\neq 0)}$. As expected, Fig. 7 (left) shows that the compression coefficient $\mathcal{C}$ increases when the wavelet prescribed threshold parameter (ϵ) increases. In the limit $\epsilon \to 0$ the compression coefficient tends to one and the computational grid converges to a uniform (regular) grid.

Finally, we check that the maximum $j_{max} = 7$ levels used in the tests are indeed sufficient to fully resolve the test function for the range of tolerances ϵ considered here. This is confirmed in Fig. 7 (right), which shows that the number of active points does not increase as when we allow more than $j_{max} = 7$.

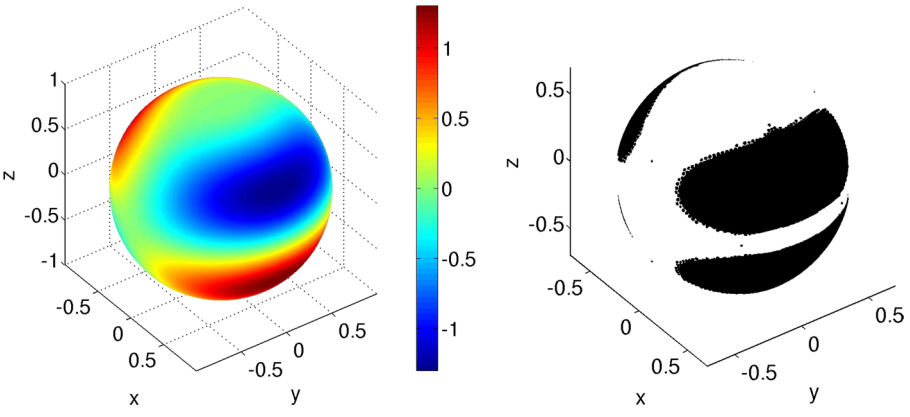

Fig. 6 Second component of gradient operator of test case 1 (*left*) and its adaptive grid (*right*)

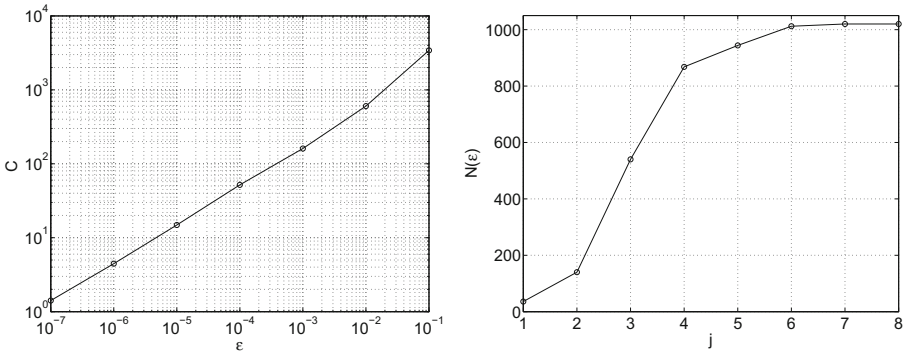

Fig. 7 Relation between compression coefficient ($\mathcal{C}$) and ϵ of second component gradient operator of test case 1 (*left*). $N(\epsilon)$ as a function of number of allowed levels j (*right*)

4.2 Test case 2

The second test case is the localized Gaussian function on the sphere

$$u(\theta, \phi) = 2 \exp\left[-\frac{(\theta - \theta_0)^2 + (\phi - \phi_0)^2}{L^2}\right], \tag{19}$$

where $\theta_0 = 0$ and $\phi_0 = 0$ and $L = 1/2\pi$. This time we show results for both first and second component of the gradient operator. The relation between ϵ and $N(\epsilon)$ is plotted in Fig. 8. The scalings of errors $||G^{1u} - G^{1u}_{\geq}||_\infty$ and $||G^{1u} - G^{1u}_{\geq}||_2$ are plotted in Figs. 9 and 10 as a function of $N(\epsilon)$ and ϵ respectively. Once again, the approximation of the gradient operator is well-controlled by the tolerance parameter ϵ.

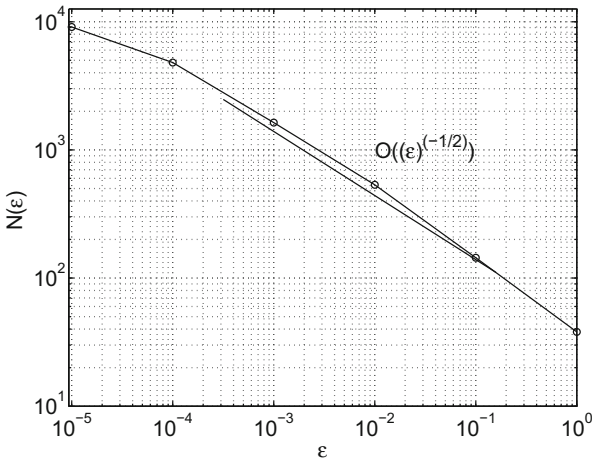

Fig. 8 Relation between number of active grid points $N(\epsilon)$ and tolerance ϵ for the first component of the gradient operator for test case 2

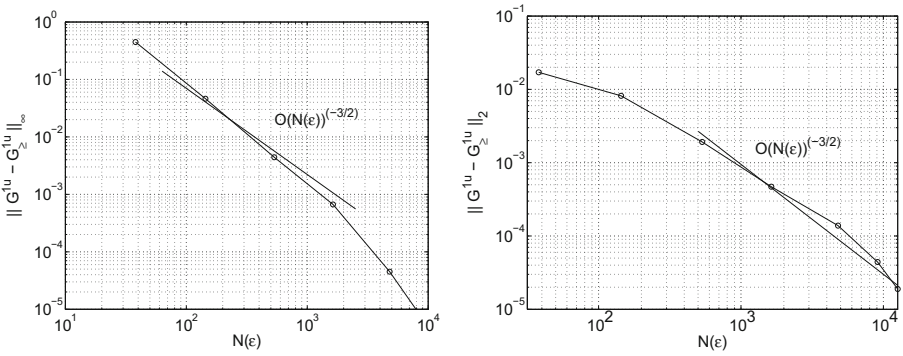

Fig. 9 Scaling of the error in the first component of the gradient operator with number of active grid points $N(\epsilon)$ in the L_∞ (*left*) and L_2 (*right*) norms for test case 2 compared with the theoretical scaling $\epsilon^{-3/2}$

Figures 11 and 12 show the two components (first and second respectively) of gradient operator for test case 2 together with the associated adaptive computational grids $\epsilon = 10^{-3}$. As in the previous test case, the adaptive grid is fine only in regions where the function has a strong gradient.

To get a better idea of how the adaptive grid tracks regions of sharp transition, we have plotted the relation between level the j and the number of active grid points $N(\epsilon)$ in Fig. 13. This figure shows that we need only up to level $j = 7$ because for $j > 7$ there is no change in the number of active points for the range of tolerances ϵ considered here. In this case the compression coefficient $\mathcal{C} \approx 22$ for $\epsilon = 10^{-2}$.

4.3 Test case 3

For the third test case we consider real turbulence data on the sphere, the real turbulence field is generated by the integration of the two-dimensional Navier-Stokes equations on the sphere without rotation after 12 hour with random seed initial condition. The field organized structures are well localized and spread on a wide range

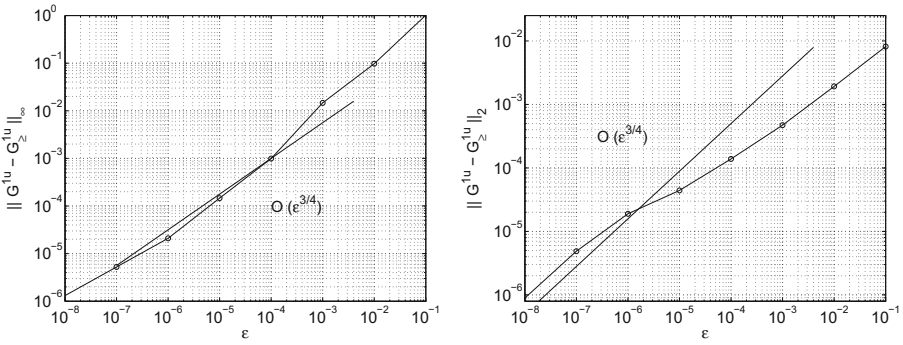

Fig. 10 Control of error for the first component of the gradient operator in the L_∞ (*left*) and L_2 (*right*) norms for test case 2 compared with the theoretical scaling $\epsilon^{3/4}$

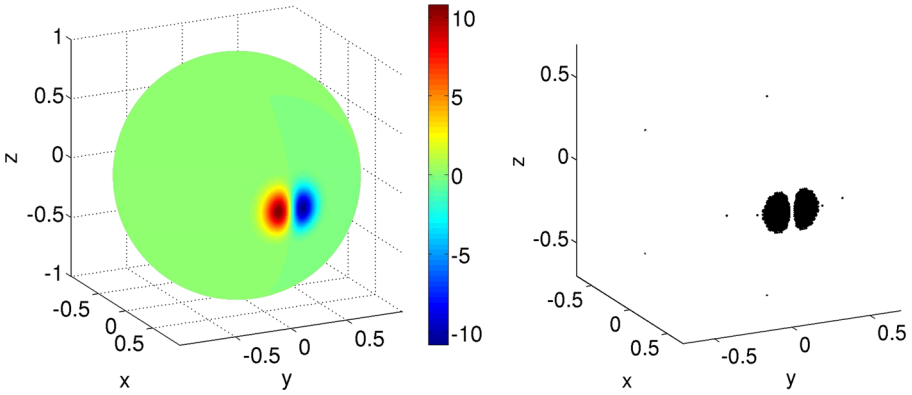

Fig. 11 First component of the gradient operator (*left*) and the corresponding adaptive grid (*right*) for test case 2 with tolerance $\epsilon = 10^{-3}$

of scales. Hence this will be a good test case for approximation of both component of gradient operator on the sphere.

We show results for both components of the gradient operator of turbulence data on a sphere. The turbulence data on the sphere is shown in Fig. 14. The first component of gradient operator is shown in Fig. 15 (left) and the associated adaptive computational grid $G_{\geq}^{1u}$ is shown in Fig. 15 (right). The second component of gradient operator is shown in Fig. 16 (left) and the associated adaptive computational grid $G_{\geq}^{2u}$ is shown in Fig. 16 (right). In the present calculation $j_{max} = 7$ for both the turbulence data and the wavelet transform. The relation between ϵ and $N(\epsilon)$ is plotted in Fig. 17, for both components of gradient operator. The scaling relations between ϵ and the error of the first and second components of the gradient operator are plotted in Fig. 18 and Fig. 19 respectively. The results indicate that in this statistically

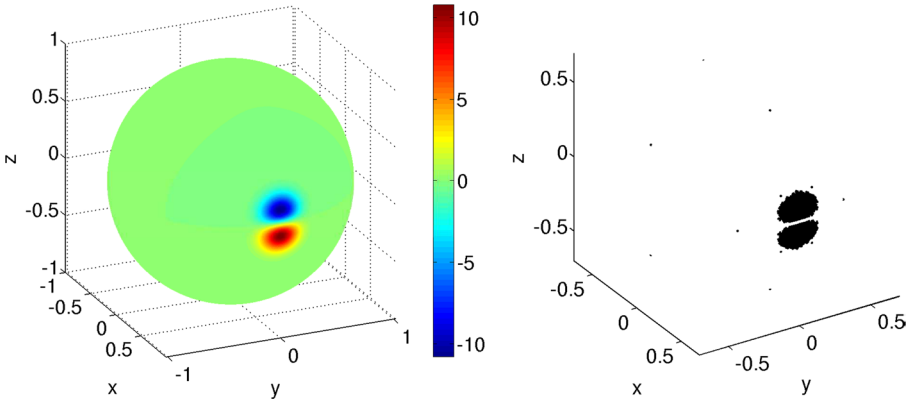

Fig. 12 Second component of the gradient operator (*left*) and the corresponding adaptive grid (*right*) for test case 2 with tolerance $\epsilon = 10^{-3}$

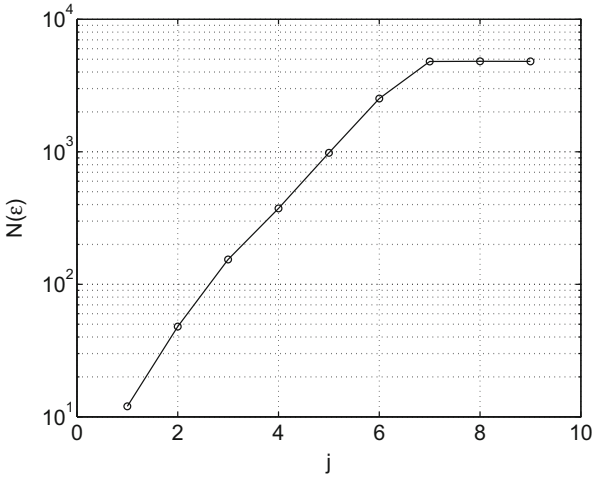

Fig. 13 Relation between the level of resolution j and number of active grid points $N(\epsilon)$ for the first component of the gradient operator for test case 2

homogeneous, but strongly multiscale case, as in the previous cases, the approximation error of the gradient operator is well-controlled by ϵ.

4.4 Test case 4 (Spherical advection equation)

We discussed multilevel approximation of the gradient operator in Section 3. Now we consider dynamic grid adaptation for the solution of linear advection problem, i.e. we incorporate our gradient scheme in a time-dependent PDE solver.

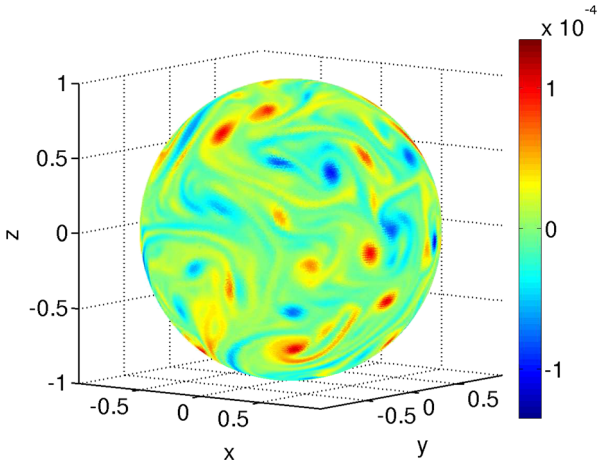

Fig. 14 Real turbulence data

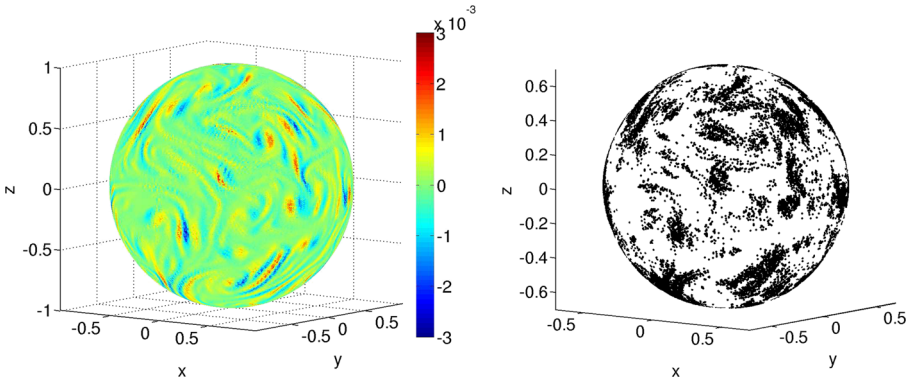

Fig. 15 First component of gradient operator (*left*) and the corresponding adaptive grid (*right*) for the turbulence data shown in Fig. 14. Note the presence of benign well-known grid-scale checkerboard oscillations in the visualization of the gradient due to the use of the C-grid [32]

Advection processes are of paramount importance in atmospheric numerical modeling. Since the fluid motions on all scales are dominated by the advection process the accurate and efficient numerical solution of the advection problem determines the overall accuracy of the ocean or atmosphere simulation. One of the main goals of this paper to apply our adaptive method for the gradient operator to standard geophysical test cases for the transport problem on the sphere [4, 33, 34]. We consider two standard geophysical test cases for linear advection driven by time-independent and time-dependent winds respectively.

When solving the time-dependent PDEs an additional criterion for grid adaptation should be added. The computational grid should consist of grid points associated with those wavelets whose coefficients are currently significant, or could become significant during a time step. In other words, at any instant in time, the computational grid should consist of the $N(\epsilon)$ significant grid points plus those grid points in an adjacent zone [18] in both position and scale that could becomes significant in one

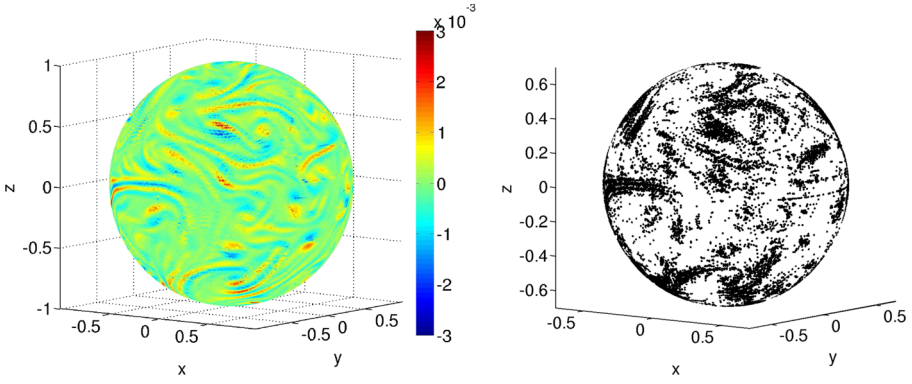

Fig. 16 Second component of gradient operator (*left*) and the corresponding adaptive grid (*right*) for the turbulence data shown in Fig. 14

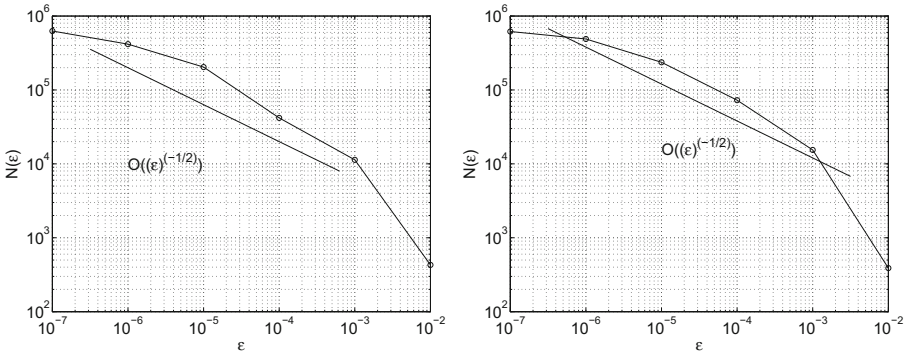

Fig. 17 Scaling of number of active grid points $N(\epsilon)$ with tolerance ϵ for the first component of gradient operator (*left*) and second component of gradient operator (*right*) for turbulence test case 3. The results are compared with the theoretical scaling $\epsilon^{-1/2}$

time step. This allows for the appearance of details on finer scales, such as shocks and localized gradients. With the addition of an adjacent zone, we have a dynamically adaptive method for time-dependent PDEs on the sphere, defined by the method of lines as a system of ordinary differential equations in time. The three basic steps are as follows:

1. Knowing the solution $u_{\geq}(t)$ on the adaptive grid, we compute the values of wavelet coefficients corresponding to each component of the solution using the fast wavelet transform. For a given threshold ϵ. we update $\mathcal{S}_{\geq}^{t+\Delta t}$ based on the magnitude of wavelet coefficients. We also add an adjacent zone [18] to the significant coefficients to allow for the change in the solution during one time step.
2. If there is no change between computational grids $\mathcal{S}_{\geq}^{t}$ and $\mathcal{S}_{\geq}^{t+\Delta t}$, we go directly to the next step. Otherwise, we interpolate the values of the solution at the collocation points $\mathcal{S}_{\geq}^{t+\Delta t}$, which are not included in $\mathcal{S}_{\geq}^{t}$.

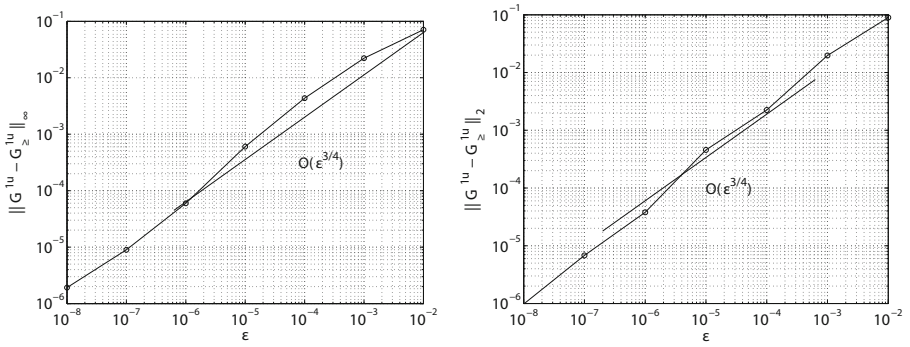

Fig. 18 Relation between $||G^{1u} - G_{\geq}^{1u}||_{\infty}$ and ϵ (left), and relation between $||G^{1u} - G_{\geq}^{1u}||_2$ and ϵ (right) for the first component of turbulence data

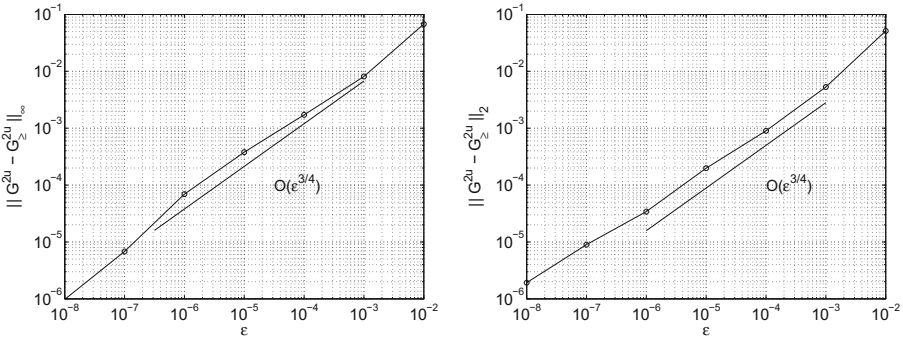

Fig. 19 Relation between $||G^{2u} - G^{2u}_{\geq}||_\infty$ and ϵ (left), and relation between $||G^{2u} - G^{2u}_{\geq}||_2$ and ϵ (right) for the second component of turbulence data

3. We integrate the resulting system of ordinary differential equations in time (e.g. using Runge–Kutta) to obtain new values to $u_{\geq}(t + \Delta t)$ at positions on adaptive grid $\mathcal{S}^{t+\Delta t}_{\geq}$, and go back to step 1.

The time integration step 3 of the above algorithm requires finite approximations of the differential operators in space that define the right hand side of the system of ordinary differential equations in time.

4.4.1 Advection of cosine bell with time-independent wind fields

In this case a cosine bell is advected once around the sphere, which is a standard test case for any numerical scheme considered for climate or weather modelling. The case was suggested by Williamson [33] to simulate the advection of a height field, $u(\theta, \phi)$ on the surface of a sphere at an angle α which is the angle between the axis of solid-body rotation and the coordinate axis of spherical coordinate system. Using adaptive wavelet collocation method [18], the partial differential equation to be solved is the spherical advection equation, which in spherical coordinates is given by

$$\frac{\partial u}{\partial t} + \mathbf{v}.\nabla u = 0, \tag{20}$$

where $t \in [0, T]$ is the time and T is the ending time of the simulation, and the advecting wind field are given by $\mathbf{v} = (v_1, v_2)$

$$\begin{aligned} v_1 &= u_0 \left[\cos(\phi)\cos(\alpha) + \sin(\phi)\cos\left(\theta + \tfrac{3\pi}{2}\right)\sin(\alpha)\right], \\ v_2 &= u_0 \sin\left(\theta + \tfrac{3\pi}{2}\right)\sin(\alpha), \end{aligned} \tag{21}$$

where u_0 the advection speed, here we set u_0 so that the rotation period is equal to one. Further, Eq. 20 can be written as

$$\frac{\partial u}{\partial t} = v_1 G^{1u} + v_2 G^{2u}.$$

The initial cosine bell test pattern that to be advected is given by,

$$u(\theta,\phi) = \begin{cases} \frac{1}{2}\left[1+\cos(\pi r/R)\right] & \text{if } r < R, \\ 0 & \text{if } r \geq R, \end{cases}$$

where $R = a/3$ and $r = a\arccos[\sin(\phi_c)\sin(\phi) + \cos(\phi_c)\cos(\phi)\cos(\theta - \theta_c)]$, which is the geodesic distance between (ϕ,θ) and the center $(\phi_c,\theta_c) = (0,0)$. We integrate Eq. 20 in time using the fourth-order Runge–Kutta method with time step $\Delta t = 10^{-4}$. The initial conditions are chosen such that $\alpha = \frac{\pi}{2} - 0.05$ (this is the most unfavourable case for latitude longitude grids). The exact solution of the advection equation at any time step is simply a translation of the initial condition, since the solid-body rotation moves the cosine bell around the globe without any shape deformation.

The initial cosine bell is plotted in Fig. 20 (left) and its associated adaptive grid is plotted Fig. 20 (right). Note that this is also the exact solution after one orbit on the non-rotating sphere. The solution of the advection equation after one complete orbit around the non-rotating sphere is shown in Fig. 21 (left) and its associated adaptive grid is shown in Fig. 21 (right). Comparing this to the exact solution (the initial condition) in Fig. 20, shows no sign of any trailing dispersive wave trains, i.e., the pattern is simply advected without changing shape as in the exact solution. The dependence of the error on the tolerance ϵ and on the number of active $N(\epsilon)$ is shown in Fig. 22 which confirms that the error is controlled by ϵ. The l_∞ error as a function of time is shown in Fig. 23. Note that in our previous approach using the Helmholtz decomposition for the flux–diffusion equation [18], some numerical dispersion was evident after one revolution in both the solution and computational grid. Thus, the present approximation represents a significant improvement both in qualitative accuracy and reduced computational cost over the previous method.

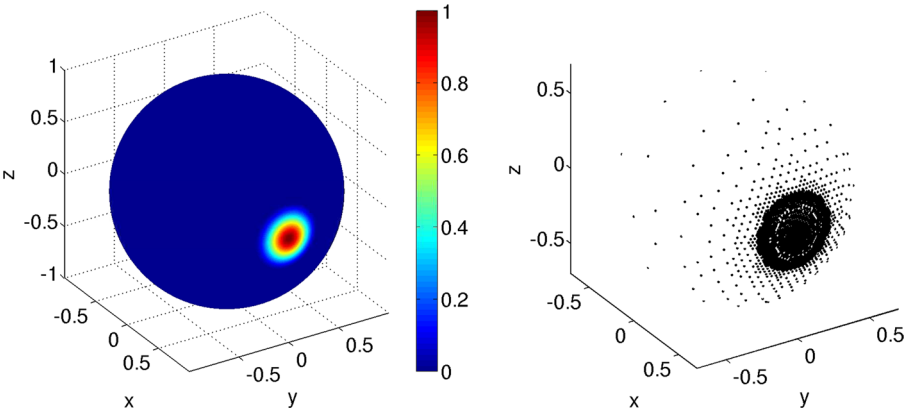

Fig. 20 Cosine bell initial conditions and exact solution after one orbit on a non-rotating sphere (*left*) and its associated adaptive grid (*right*)

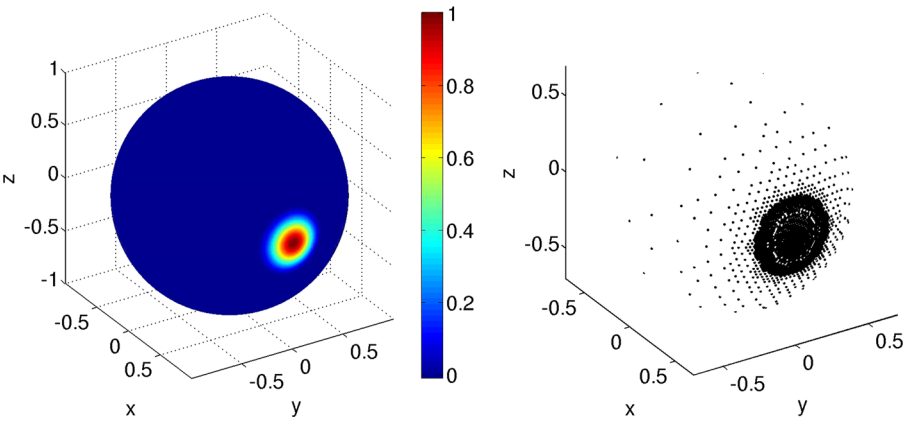

Fig. 21 Numerical solution of the advection of cosine bell test case after one orbit on a non-rotating sphere (*left*) and its associated adaptive grid (*right*)

4.4.2 Advection of cosine bells with time-dependent wind fields

We now consider the advection of two symmetric cosine bells for the time-dependent wind test case proposed in [4]. The spatial and temporal structure of the velocity vector $\mathbf{V}(\theta, \phi, t) = (v_1(\theta, \phi, t), v_2(\theta, \phi, t))$ is

$$\begin{aligned} v_1 &= 2\sin^2(\theta)\sin(2\phi)\cos(\pi t/T), \\ v_2 &= 2\sin(2\theta)\cos(\phi)\cos(\pi t/T). \end{aligned} \tag{22}$$

The symmetric cosine bell initial condition $u(\theta, \phi)$ is

$$u(\theta,\phi) = \begin{cases} b + cu_1(\theta,\phi) & if r_1 < R, \\ b + cu_2(\theta,\phi) & if r_2 < R, \\ b & otherwise, \end{cases} \tag{23}$$

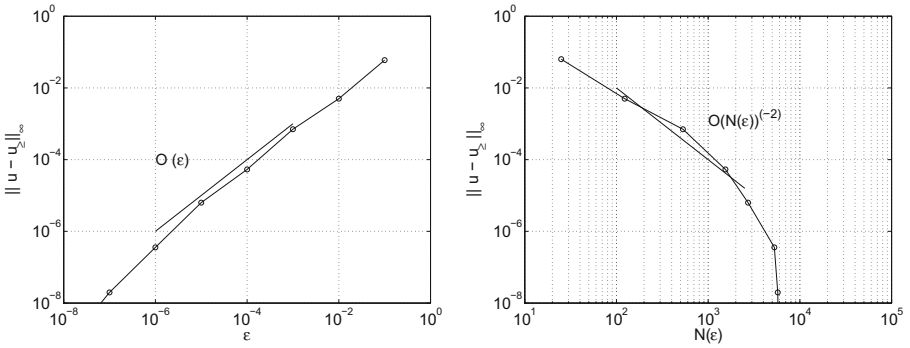

Fig. 22 Error convergence as a function of tolerance ϵ (*left*) and as a function of number of active grid points $N(\epsilon)$ (*right*) for the solution of advection of cosine bell

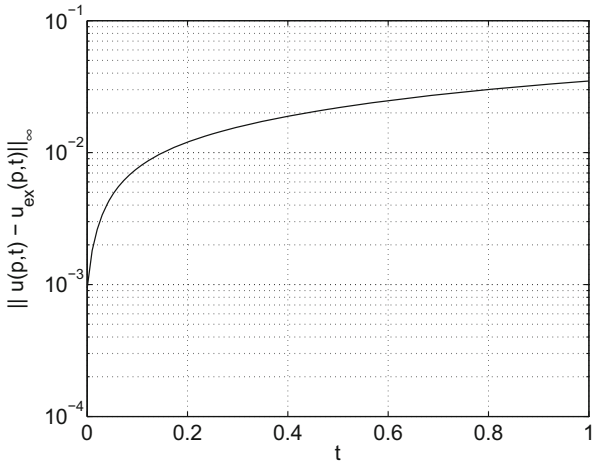

Fig. 23 Point wise (L_∞) error of the advected cosine bell solution as a function of time

where the background value $b = 0$ and amplitute $c = 1$, such that $u \in [0, 1]$. The initial position of the distribution $u_i = u(\theta_i, \phi_i, t)$ with $i = 1, 2$, is

$$u_i(\theta, \phi) = \frac{h_{\max}}{2} [1 + \cos(\pi r_i / R)] \quad \text{if } r_i < R. \tag{24}$$

where the amplitude $h_{\max} = 1$, base radius $R = a/3$, and great circle distance between (θ, ϕ) and the center (θ_i, ϕ_i) is $r_i = r_i(\theta, \phi) = a \arccos[\sin(\phi_i)\sin(\phi) + \cos(\phi_i)\cos(\phi)\cos(\theta - \theta_i)]$, where $(\theta_1, \phi_1) = (\pi/6, 0)$ and $(\theta_2, \phi_2) = (-\pi/6, 0)$. The initial condition is plotted in Fig. 24 (left) and its associated adaptive grid is plotted Fig. 24 (right).

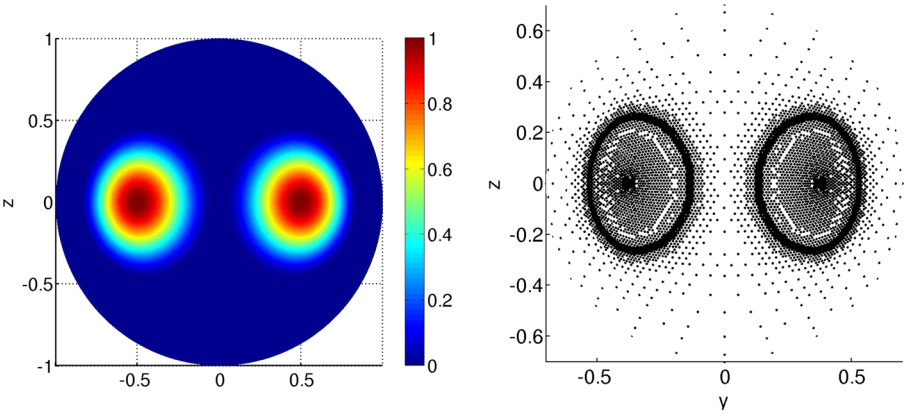

Fig. 24 Cosine bells initial conditions and exact solution after time $T = 5$ on a non-rotating sphere (*left*) and its associated adaptive grid (*right*)

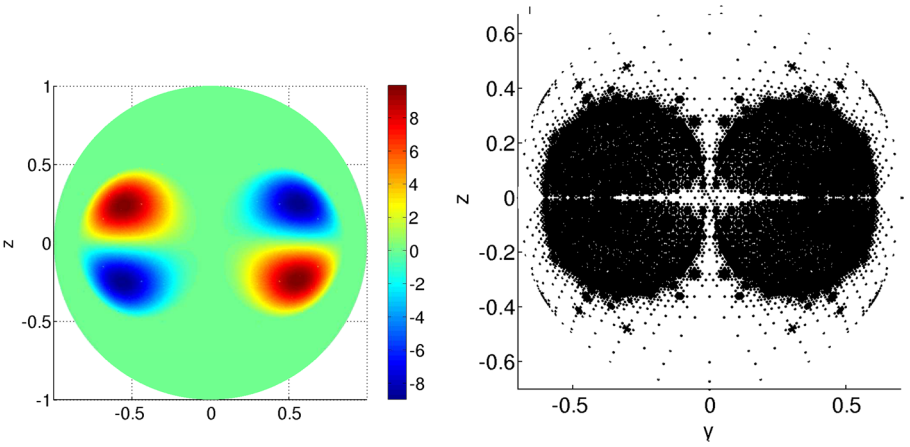

Fig. 25 Numerical solution of the advection of cosine bells at time $t = 2.5$ (*left*) and its associated adaptive grid (*right*)

The advection Eq. 20 is integrated with time-dependent velocity vector (22) and initial profile (23) in time using the fourth-order Runge–Kutta method with time step $\Delta t = 10^{-4}$. The exact solution of this test case at time $T = 5$ is identical to the initial condition although, unlike the previous time-independent wind case, the solution is different at intermediate times. As time increases the cosine bells are increasingly deformed into spiral shapes until at time $t = T/2$ the field is maximally deformed and has split into four pieces as shown in Fig. 25. The solution should return exactly to the initial double cosine bell state at $t = 5$. Comparing Fig. 24 to the numerical solution at $t = 5$ shown in Fig. 26 shows the good qualitative accuracy of the dynamically adaptive wavelet method for this challenging transport test. More qualitatively, we also show contour plots of the solution at three times in Fig. 27. As in the simpler

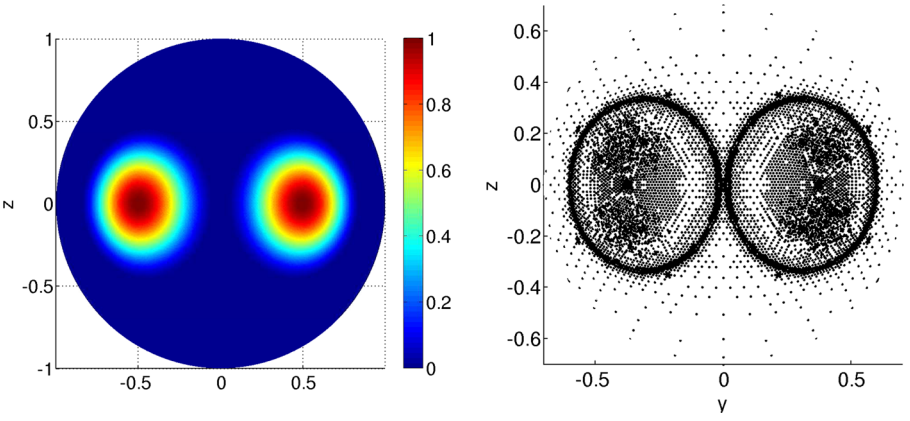

Fig. 26 Numerical solution of the advection of cosine bells at time $t = 5$ when cosine bells return back to the initial position (*left*) and its associated adaptive grid (*right*)

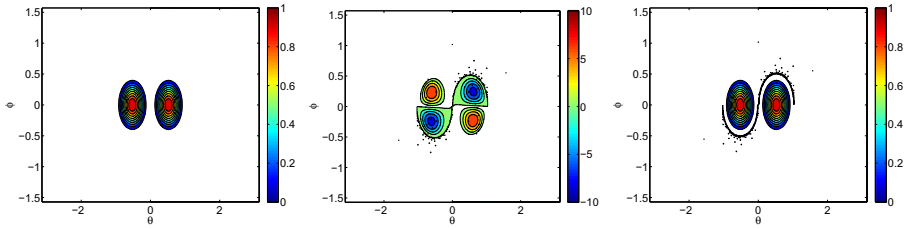

Fig. 27 Contour plots of cosine bells initial conditions and exact solution after time $t = 5$ on a non-rotating sphere (*left*), numerical solution of the advection of cosine bells at time $t = 2.5$ (*middle*), and numerical solution of the advection of cosine bells at time $t = 5$ when cosine bells return back to the initial position (*right*)

time-independent case, there is no sign significant numerical dispersion of the solution or grid. The only difference is that the grid for the solution at $t = 5$ is slightly larger than than of the initial condition, although the numerical solutions is essentially identical.

The accuracy is measured using l_∞ error, which is computed at the end of the simulation $t = T$ when the exact solution is known (i.e., it equals the initial condition). Numerical convergence is verified by progressively decreasing the threshold parameter ϵ. We the dependence of the error on the tolerance ϵ and on the number of active grid points $N(\epsilon)$ Fig. 28. These results confirm convergence and that the errors are indeed controlled by ϵ and $N(\epsilon)$.

These results show that our dynamically adaptive gradient approximation method is both qualitatively and quantitatively accurate, and is able to track the reversible deformation generated by the time-dependent advecting velocity field. It is thus well-suited to ocean and atmosphere simulation where accurate and efficient non-dispersive and non-diffusive computation of transport problems is essential.

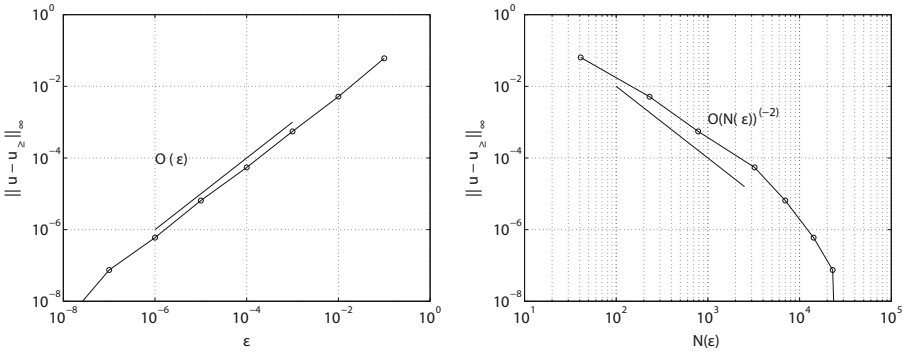

Fig. 28 Error convergence as a function of tolerance ϵ (*left*) and number of active grid points $N(\epsilon)$ (*right*) for the solution of advection of cosine bells

5 Summary and future work

This paper introduces a new wavelet-based multilevel approximation of gradient and advection operators on an adaptive spherical geodesic grid. This new method, unlike our previous flux–divergence form [18], does not require computing the Helmholtz–Hodge decomposition and appears not to suffer from numerical dispersion in either the solution or dynamically adapted computational grid. Since computation of gradient operators is necessary for many applications in data analysis and in the numerical simulation of PDEs on the sphere, this efficient and accurate new technique should be practically useful.

The theoretical properties of the scheme are verified by applying it to the localized test function proposed by Heikes & Randall [21], a Gaussian function on the sphere, and a real turbulence data. Finally, the gradient operator approximation is implemented in a dynamically adaptive linear advection solver. This solver is then applied to a standard geophysical test case for time-independent [33] transport and a more recent and more challenging test case for deformational time-dependent transport on the sphere [4].

Our approach is based on second-generation wavelets which means it can be custom designed for general curved complex domains and irregular sampling. The high resolution computations are performed only in regions where sharp transitions occur. Thus, the strength of this method is that it can be generally applied in atmospheric and geophysical simulation problems (e.g. on the geoid rather than a perfect sphere), computational fluid dynamics and turbulence flow while retaining the freedom and flexibility to select the wavelet basis best-suited to the specific application.

Acknowledgments MM acknowledges the support provided by Department of Science and Technology, India, under the grant number *RP*02417 and would also like to thank Dr. Olivier Pannekoucke for providing the turbulence data on the sphere. NKRK acknowledges the support of an NSERC Discovery Grant.

References

1. Sbalzarini, I.F., Hayer, A., Helenius, A., Koumoutsakos, P.: Simulations of anistropic diffusion on curved biological surfaces. Biophys. J. **90**, 878–885 (2006)
2. Novak, I.G., Gao, F., Choi, Y.S., Resasco, D., Schaff, J.C., Slepchenko, B.M.: Diffusion on a curved surface coupled to diffusion in the volume: Application to cell biology. J. Comput. Phys. **226**, 1271–1290 (2007)
3. Nair, R.D., Jablonowski, C.: Moving vortices on the sphere: A test case for horizontal advection problems. Mon. Wea. Rev. **136**(2), 699–711 (2007)
4. Nair, R.D., Lauritzen, P.H.: A class of deformational flow test cases for linear transport problems on the sphere. J. Comput. Phys. **229**(23), 8868–8887 (2010)
5. Farid, H., Simoncelli, E.P.: Differentiation of discrete multidimensional signals. IEEE Trans. Image Process. **13**(4), 496–508 (2004)
6. Shima, T., Saito, S., Nakajima, M.: Design and evaluation of more accurate gradient operators on hexagonal lattices. IEEE Trans. Pattern. Anal. Mach. Intell. **32**(6), 961–973 (2010)
7. Gan, R., Chung, A.C.S., Liao, S.: Maximum distance - gradient for robust image registration. Med. Image Anal. **12**, 452–468 (2008)
8. Ben-yu, G.: A spectral method for the voriticity equation on the surface. Math. Comp. **64**, 1067–1079 (1995)

9. Daubechies, I.: Ten lectures on Wavelets. SIAM (1992)
10. Meyer, Y.: Analysis at Urbana I: Analysis in Function Spaces. Cambridge University Press, Cambridge (1989)
11. Sweldens, W.: The lifting scheme: A construction of second generation wavelets. SIAM J. Math. Anal. **2**(29), 511–546 (1998)
12. Vasilyev, O.V., Bowman, C.: Second generation wavelet collocation method for the solution of partial differential equations. J. Comput. Phys. **165**, 660–693 (2000)
13. Vasilyev, O.V., Paolucci, S.: A dynamically adaptive multilevel wavelet collocation method for solving partial differential equations in a finite domain. J. Comput. Phys. **125**(111), 498–512 (1996)
14. Roussel, O.V., Schneider, K., Tsigulin, A., Bockhorn, H.: A conservative fully adaptive multiresolution algorithm for parabolic PDEs. J. Comput Phys. **188**(2), 493–523 (2003)
15. Roussel, O.V., Schneider, K.: Coherent vortex simulation of weakly compressible turbulent mixing layers using adaptive multiresolution methods. J. Comput. Phys. **229**, 2267–2286 (2010)
16. Domingues, M.O., Gomes, S.M., Roussel, O., Schneider, K.: An adaptive multiresolution scheme with local time stepping for evolutionary PDEs. J. Comput. Phys. **227**, 3758–3780 (2008)
17. Schneider, K., Vasilyev, O.V.: Wavelet methods in computational fluid dynamics. Annu. Rev. Fluid Mech. **42**, 473–503 (2010)
18. Mehra, M., Kevlahan, N.K.R.: An adaptive wavelet collocation method for the solution of partial differential equation on the sphere. J. Comput. Phys **227**, 5610–5632 (2008)
19. Mehra, M., Kevlahan, N.K.R.: An adaptive multilevel wavelet solver for elliptic equations on an optimal spherical geodesic grid. SIAM J. Sci. Comput. **30**(6), 3073–3086 (2008)
20. Behera, R., Mehra, M.: Integration of barotrophic vorticity equation over spherical geodesic grid using multilevel adaptive wavelet collocation method. Appl. Math. Modelling **37**, 5215–5226 (2013)
21. Heikes, R., Randall, D.A.: Numerical integration of the shallow-water equations on a twisted icosahedral grid. part: Basic design and results of test. Mon. Wea. Rev. **123**, 1862–1880 (1995)
22. Williamson, D.L.: Integration of the barotrophic vorticity equation on a spherical geodesic grid. Tellus **4**, 642–653 (1968)
23. Sadourny, R., Akakawa, A., Mintz, Y.: Integration of the nondivergent barotropic vorticity equation with an icosahedral-hexagonal grid for the sphere. Mon. Wea. Rev. **96**, 351–356 (1968)
24. Masuda, Y., Ohnishi, H.: Short and medium Renge Numerical Weather Predication: Meteorological Society of Japan. In: Matsuno, T. (ed.): An integration scheme of the primitive equation model with a icosahedral-hexagonal grid system and its application to the shallow water equations, pp. 317–326 (1986)
25. Pudykiewicz, J.A.: Numerical solution of the reaction-advection-diffusion equation on the sphere. J. Comput. Phys. **213**, 358–390 (2006)
26. Schroder, P., Sweldens, W.: In Proceedings of the 22nd Annual Conference on Computer Graphics and Interactive Techniques: Spherical wavelets: Efficiently representing functions on the sphere, pp. 161–172 (1995)
27. Tomita, H., Tsugawa, M., Satoh, M., Goto, K.: Shallow water model on a modified icosahedral geodesic grid by using spring dynamics. J. Comput Phys. **174**, 579–613 (2001)
28. Meyer, M., Desbrun, M., Schroder, P., Barr, A.: Visualization and Mathematics III: Discrete differential geometry operator for triangulated 2-manifolds, pp. 35–57 (2002)
29. Donoho, D.L.: Interpolating wavelet transforms. Technical Report 408, Department of Statistics, Stanford University (1992)
30. Vasilyev, O.V.: Solving multi-dimensional evolution problems with localized structure using second generation wavelets. Int. J. Comp. Fluid Dyn. **17**(2), 151–168 (2003)
31. Dyn, N., Levin, D., Gregory, J.: A butterfly subdivision scheme for surface interpolation with tension control. Trans. Graph. **9**(2), 160–169 (1990)
32. Gassmann, A.: Inspection of hexagonal and triangular c-grid discretizations of the shallow water equations. J. Comput. Phys. **230**(7), 2706–2721 (2011)
33. Williamson, D.L., Drake, J.B., Hack, J.J., Jacob, R., Swarztrauber, P.N.: A standard test set for numerical approximations to the shallow water equations in spherical geometry. J. Comput. Phys. **102**, 211–224 (1992)
34. Lauritzen, P.H., Skamarock, W.B., Prather, M.J., Taylor, M.A.: A standard test case suite for two-dimensional linear transport on the sphere. Geosci. Model Dev. **5**, 887–901 (2012)